A particle-based approach to predict the success and selectivity of leaching processes using ethaline - Comparison of simulated and experimental results

Chandra Widyananda Winardhi, Jose Ricardo da Assuncao Godinho, Cindytami Rachmawati, Isabelle Duhamel-Achin, Ainhoa Unzurrunzaga Iturbe, Gero Frisch, Jens Gutzmer

Hydrometallurgy 211 (2022) 105869

Contents lists available at ScienceDirect

Hydrometallurgy

journal homepage: www.elsevier.com/locate/hydromet

A particle-based approach to predict the success and selectivity of leaching processes using ethaline - Comparison of simulated and experimental results

Chandra Widyananda Winardhi [a,*], Jose Ricardo da Assuncao Godinho [a], Cindytami Rachmawati [a], Isabelle Duhamel Achin [b], Ainhoa Unzurrunzaga Iturbe [c], Gero Frisch [d], Jens Gutzmer [a]

[a] Helmholtz Zentrum-Dresden Rossendorf, Helmholtz Institute Freiberg for Resource Technology, 09599 Freiberg, Germany
[b] Bureau de Recherches Géologiques et Minières (BRGM), F-45060 Orléans, France
[c] Fundacion Tecnalia Research and Innovation, Paseo Mikeletegi 2, 20009 San Sebastián, Spain
[d] Institut für Anorganische Chemie, Technische Universität Bergakademie Freiberg, 09599 Freiberg, Germany

ARTICLE INFO

Keywords:
Computed tomography (CT)
Dissolution rates
Deep eutectic solvents
Leaching
Particle-based leaching simulation

ABSTRACT

Encouraged by the need for ecologically and economically sustainable technologies for the recovery of metals from complex raw materials, ionometallurgical leaching using deep eutectic solvents is emerging as a promising alternative to conventional hydro- and pyrometallurgical process routes. Current approaches of studying leaching processes do not provide a mineral-based understanding of the leaching process – thus limiting the opportunities for process optimization. This study addresses this shortcoming by combining laboratory-based X-ray computed tomography (CT) and scanning electron microscopy-based image analysis. The latter method provides precise information on the mineralogy and texture of the leach feed material, whereas CT is used to observe the progress of the leaching process through time. Leaching of Au—Ag bearing sulfide flotation concentrate by the deep eutectic solvent ethaline with iodine as oxidizing agent is used as a relevant case study. Results show that time-lapse CT provides an accurate estimation of the dissolution rate of pyrite, chalcopyrite, galena, telluride minerals and gold. Dissolution rates were used to simulate the metal recoveries from the sulfide concentrate as a function of leaching time. Simulation results are within 5% variation of metal recoveries obtained by batch leaching experiments. The developed workflow can be easily transferred to other ore types or mineral concentrates; results may be used to study and optimize industrial leaching processes.

1. Introduction

The global transition to renewable energy sources as well as the need to reduce CO_2 emissions in order to limit global climate change (Kalair et al., 2021) invariably results in an increasing demand for a large suite of inorganic raw materials, e.g. minerals and metals. Technological routes for metals extraction include many solution-based processes, which are energy-efficient (Anthony and Flett, 1994) but require the use of large volumes of water as a solvent (Gaydardjiev, 1998). In order to reduce water consumption, the use of ionic liquids as solvent has been suggested (Abbott et al., 2003; Jenkin et al., 2016). However, conventional ionic liquids are often costly and difficult to recover (Zhou et al., 2018) – their use as a solvent in the raw materials industry has thus often not been deemed economically feasible. Deep eutectic solvents (DESs) are, however, have emerged as cost-efficient solvents (Smith et al., 2014); they have low melting points (Abbott et al., 2004; Abbott et al., 2006; Zhou et al., 2018), are typically biodegradable (Radošević et al., 2015) and may be more selective towards leaching specific metals (Abbott et al., 2006; Jenkin et al., 2016; Zürner and Frisch, 2019; Rodriguez et al., 2020).Yet, little is currently known about the actual leaching process and the interaction of DESs with various mineral species composing a complex ore.

Leaching of minerals is a dynamic process that largely depends on the physicochemical properties of the mineral assemblage e.g. the minerals present, their intergrowth, mineral grain and particle sizes and the reactive surface area of each mineral present. Yet, traditional

* Corresponding author.
E-mail address: c.winardhi@hzdr.de (C.W. Winardhi).

https://doi.org/10.1016/j.hydromet.2022.105869
Received 7 December 2021; Received in revised form 18 March 2022; Accepted 28 March 2022
Available online 4 April 2022

approaches to investigate the leaching of ores have typically been limited to measuring element concentrations in the leachate and in the solid feed and residue materials (Ilhan and Akgün, 2021; Dávila-Pulido et al., 2021). Other tangible properties of the minerals and the dynamics of mineral-fluid interactions are often ignored- though 3D surface imaging methods were used in some previous studies. Time-resolved 3D surface measurements using an optical profiler (Godinho et al., 2012; Jenkin et al., 2016; Saldi et al., 2017) or an atomic force microscope (Godinho et al., 2014; Wang and Putnis, 2020) were successfully used to determine dissolution rates based on surface retreat at nanometer scale resolution. However, despite providing high spatial resolution, these methods usually require flat polished surfaces and are restricted to very small fields of view.

As an alternative to time-resolved 3D surface methods, time-resolved non-destructive and non-invasive X-ray computed tomography (CT) can be used to directly image changes during reactive fluid-mineral interaction (Dewanckele et al., 2012; Lin et al. 2016; Noiriel et al., 2020). From 3D images the properties of the material can be directly measured, including, for example, surface area and volume of grains. This allows the calculation of dissolution rates normalized to the surface area of a specific mineral (Noiriel et al., 2009; Godinho et al., 2016). Laboratory CT scanners are now widely available and offer a larger scale of observation (Lin et al., 2016a; Lin et al., 2016b; Godinho and Withers, 2018). Despite these obvious advantages, laboratory-based CT cannot provide sufficient spatial and mineralogical information necessary to analyze complex particle microstructures typical of ores and ore mineral concentrates that are typically encountered in industrial leaching operations (Wills and Finch, 2015; Godinho et al., 2019). As a source for such quantitative mineralogical and textural observation, SEM-based 2D image analysis which often referred to as “automated mineralogy”, Schulz et al., 2019, can be used as an alternative. Correlation between CT and automated mineralogical data has been carried out to overcome the limitations of both methods to provide robust constraints on mineralogy and texture of mineral raw materials in 3D space (Godinho et al., 2021).

In this study, a novel workflow is introduced to monitor the leaching of complex raw materials in DESs using laboratory-based CT instrumentation in combination with mineralogical data obtained by SEM-based image analysis. Changes of volume and surface area changes of particles are recorded through time and used to calculate mineral specific dissolution rates. For this purpose, individual and monomineralic grains of ore minerals were leached using a DES in a first step in order to calculate dissolution rates. These dissolution rates were then used to simulate the leaching of complex and polymineralic particles from a real mineral concentrate. The composition of this concentrate was constrained by SEM-based image analysis (2D imaging). The results of this simulation was finally used to estimate metal recoveries over time. Our new method was validated by comparing the simulation results to metal recoveries obtained during conventional batch leaching experiments on the same mineral concentrate.

2. Materials and method

In this study, a simulation code was developed to model the leaching process that allows to optimize and to predict mineral leaching and metal leaching efficiency as a function of time. The simulation input variables are: 1) The dissolution rate of the minerals of interest - calculated using direct measurements of the changes of volume and surface area of minerals lost over time using CT. 2) The reactive surface area of each mineral of interest was derived from 2D images obtained by MLA. 3) Leaching time to calculate global mineral leaching based on the observed mineral assemblages.

2.1. Materials

The material used in this study was a gold-bearing sulfide concentrate from the Cononish gold mine in the Scottish Highlands, currently operated by Scotgold Resources Ltd. The mineral concentrate was obtained by conventional froth flotation with size fraction below 212 μm; the sample material was supplied by Wardell Armstrong (UK). The Cononish deposit is a quartz vein-hosted Au—Ag deposit with an average grade of 47.7 g/t silver and 11.1 g/t gold (Cononish Project: Scotgold Resources Ltd., 2021). The Cononish deposit is also known to be rich in tellurium, with a Te/Au molar ratio of 2.4.

2.2. Sample characterization

Five subsamples weighing 2 g each were obtained from the original sulfide concentrate sample using a rotary sample splitter. Each sample was mixed with graphite and epoxy to prepare a 30 mm in diameter grain mount. From that, so-called T-sections (Heinig et al., 2015) were prepared using standardized procedures. Surface of the T-Sections were then plane polished down to 1 μm sized using a micro-diamond drape. The mineral assemblage embedded in the polished T-sections were characterized using a Mineral Liberation Analyzer (MLA, FEI Company, Hilsboro, OR, USA) based on a FEI Quantax 650F field emission scanning electron microscope equipped with two Bruker Quanta X-Flash 5030 energy dispersive X-ray detectors (EDX). The grain-based X-ray mapping (GXMAP) measurement mode was used (Fandrich et al., 2007) and back-scattered electron (BSE) images were acquired with a resolution of 6 μm/pixel and 1 μm/pixel respectively. Mineral classification was done with the MLA Suite software package 3.1.4.686 (MLA Image Processing and MLA Mineral Reference Editor). A modified approach for mixed spectra was applied during processing as described by Kern et al. (2019).

The chemical composition of the ore minerals, e.g., the minerals containing the valuable elements in question were analyzed at BRGM Laboratory using an electron microprobe CAMECA-SX equipped with five wavelength-dispersive spectrometers (WDS) and owned jointly by the French Geological Survey and ISTO University in Orleans. Polished thin sections of the ore and flotation concentrates were carbon-coated with a thickness of approximately 20 nm using a CRESSINGTON 308 carbon coater. The quantitative major and trace element contents for each mineral were determined by in situ electron microprobe analyses (EPMA). EPMA was performed with an accelerating voltage of 20 kV, a beam current of 50 nA, and a 1 μm beam diameter. The system was calibrated with a selection of natural minerals and synthetic phases and pure elements: S and Fe on FeS_2, Ni on Ni (metal), Co on Co (metal), Cu on Cu (metal), Zn on ZnS, Ga and As on AsGa, Ag on Ag (metal), Au on Au (metal), In on roquesite ($CuInS_2$, Picot and Pierrot, 1963), Sb on stibnite (Sb_2S_3), Te on Te metal, Pb on PbS, Sn on SnO_2, Se on PbSe, Bi on $Bi_{19}I_3S_{27}$ (Miehe and Kupčík, 1971). Interferences were corrected for Pb Lα interfering Bi Lα (Cameca Peak-Sight software). The φ(ρZ) method X-Phi (Merlet 1992 and 1994) was used for intensity correction. Mean detection limits calculated according to Ancey and Bastenaire model (Ancey et al., 1978) were about 560 g/t for Te, 1900 g/t for Au and 730 g/t for Ag. The accurate composition of the minerals was determined using comparison with both natural and synthetic standards. The counting time was between 5 and 30 s per element, the longer time being used for the low concentrations and especially to obtain a higher precision on the determination of the Pb contents. Relative errors on element concentrations are expected to be below 1%. Averaged electron microprobe mineral compositions were used to construct the mineral chemistry data base of the MLA.

Aliquots of the sulfide concentrate were also analyzed at Tecnalia Laboratory by inductively coupled plasma mass spectrometry (ICP-MS) for their bulk chemical composition. Seven samples of approximately 0.1 g of the sulfide concentrate were digested in 2 mL of concentrated nitric acid (65%), 6 mL hydrochloric acid (37%) and 2 mL of hydrofluoric acid (48%) by using a Milestone Ethos Up Microwave Digestion System. Both sample and acid mixture were placed in an inert PTFE sealed microwave vessels. The temperature profile was set to reach 230 ± 10 °C within 20 min followed by 15 min of holding time. Then, 25 mL

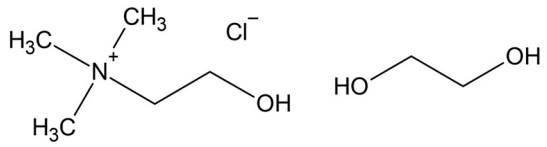

Fig. 1. Chemical formula of ethaline which consists of choline chloride ($HOC_2H_4N(CH_3)_3Cl$) and ethylene glycol ($HOCH_2CH_2OH$).

Table 1
Origin of samples used for single particle leaching.

Sample / Mineral	Details / Origin	Provider
Hessite (Ag_2Te)	Nagyag, Romania	Geoscientific Collections of TU Bergakademie Freiberg
Sylvanite ($(Au,Ag)_2Te_4$)	Nagyag, Romania	
Acanthite (Ag_2S)	Freiberg, Germany	
Galena (PbS)	Skellefte, Sweden	Helmholtz Institute Freiberg
Chalcopyrite ($CuFeS_2$)	Durango, Mexico	
Pyrite (FeS_2)	China	
Gold (Au)	Technical Product	Sigma-Aldrich

of 4% boric acid was added in order to complex the HF excess. The heating program used in this case was set to reach 180 ± 10 °C in 20 min followed by 15 min holding time. After cooling, the vessel content was diluted to 50 mL by using distilled water and then analyzed.

2.3. Single particle leaching experiments

The leaching fluid ethaline was prepared by mixing 1:2 M ratio of choline chloride (ChCl, Sigma Aldrich, >98%) with ethylene glycol (EG, Merck, >98%) (Fig. 1) and 100 mM of iodine (Sigma Aldrich) as oxidizing agent (Abbott et al., 2015).

The oxidant role in gold case was to catalyst gold to ions (1) (Jenkin et al., 2016) and for other minerals to oxidize sulfide and telluride.

$$2Au + I_2 = 2Au^+ + 2I^- \quad (1)$$

The solution was stirred at 500 rpm and heated to 50 °C. Leaching was done on single particles comprising only of one of each mineral of interest. Prior to leaching, each particle was scanned by CT. Each particle was then leached for a specific time in a stirred leaching reactor. At the end of the predefined leaching time, the particle was removed from the fluid and rinsed with ethanol to stop the leaching process. Then, the particle was again scanned by CT.

Minerals selected for leaching are those that were identified during mineralogical studies of the sulfide concentrate from the Cononish deposit to contain the three target elements Au, Ag and Te as well as three quantitatively important sulfide gangue minerals (Table 1). The actual mineral grains chosen for the leaching experiments were well documented examples from the collections as listed in Table 1. Hessite was chosen as the main bearing silver-gold-telluride mineral and acanthite as silver sulfide. For the lack of alternatives, petzite (Ag_3AuTe_2), which is present in the sulfide concentrate from Cononish Mine, was substituted by sylvanite ($(Au, Ag)Te_2$). Instead of electrum (a natural (Au, Ag) alloy of variable composition) a commercially available gold sphere was used for the leaching experiments. Pyrite (FeS_2), chalcopyrite ($CuFeS_2$) and galena (PbS) are quantitatively important sulfide minerals in the concentrate. Quartz (SiO_2) was not studied as it is well known to remain insoluble in ethaline solution as described by (Abbott et al., 2004).

Gold, acanthite, and hessite were leached for 2 h, sylvanite for 3 h, galena and chalcopyrite for 20 h and pyrite for 90 h. Different leaching time was chosen due to the expected differences in leaching kinetics for each mineral in combination with the limitation of CT resolution to distinguish the difference prior to leaching and after leaching. All particles were leached at 50 °C and 500 rpm (except sylvanite, galena and pyrite that were leached at 300 rpm to prevent the particle to break).

2.4. Computed tomography (CT)

Samples were scanned using a XRE CoreTOM (Tescan) instrument with a voxel size of 4.65 μm. Two different scanning parameters were used depending on the sample. Sample with low attenuation, chalcopyrite and pyrite was scanned using 160 keV accelerating voltage, 15 W power, 1 s, and a 2 mm copper filter mounted at the source. The sample with high attenuation were scanned using 180 keV accelerating voltage, 15 W power, 1 s exposure time and a 50 μm tungsten filter mounted at the source to reduce image artifacts. Radiographs were reconstructed using Acquila 1.0.0.70 reconstruction software by Tescan. The 3D images were processed in Avizo 9.2.0 using a non-local means filter to reduce noise, followed by segmentation using an Otsu algorithm. Bulk volume and surface area were calculated from the binary image. The specific dissolution rate (k) was calculated using Eq. (2) (Godinho and Stack, 2015) by dividing the volume variation ($V_{ti} - V_{ti+1}$) by the time interval ($t_{i+1} - t_i$) and by the average surface area between the initial and final surfaces ($A_{ti,\ ti+1}$).

$$k_i = \left(\frac{V_{t_i} - V_{t_{i+1}}}{t_{i+1} - t_i}\right) \frac{1}{\overline{A_{t_i,t_{i+1}}}} \quad (2)$$

2.5. Particle-based leaching simulation

The simulation code was developed using MATLAB MathWorks as illustrated in Fig. 2. Mineral liberation analysis provides images of classified particles as an input (Fig. 2b). From these images, the liberated / exposed surface of each mineral of interest present in a particle can be identified as the surface between the mineral grains of interest and the epoxy resin. This surface (pink and green pixels, Fig. 2c) provides initial access to the leaching agent. Leaching may be graphically represented by the successive disappearance of exposed pixels. The reactive surface boundary is updated in each iteration according to the dissolution rate calculated from Eq. (1). Internal mineral surfaces are unreactive during the simulation (red line, Fig. 2c) until it get exposed.

In the simulation, the MLA mineral list was simplified by grouping the different gangue sulfides mineral (except chalcopyrite and pyrite) and assigning to this group the same dissolution rate as chalcopyrite. Gangue minerals of no further interest for this study were grouped together and classified as unreactive minerals - similar to quartz. The simulation took around 17 h of computing time to simulate 96 h of leaching. From a total of 943,875 particles measured by MLA, only 322,842 particles were found to contain electrum, hessite, petzite, acanthite, galena, chalcopyrite and pyrite as minerals of interest. Only these particles were considered in the leaching simulation, while all others were deemed to be inert. The results of this leaching simulation is a measure of cumulative mineral leaching at a given time. The mineral leaching (%) was then calculated using Eq. (3) by dividing the simulated cumulative mineral (m) leaching result at each time ($\sum_t A_t^m$) to the total mineral area characterized by MLA ($A_{total}{}^m$).

$$Mineral\ leaching\ (\%) = \frac{\sum_t A_t^m}{A_{total}^m} x\ 100\% \quad (3)$$

This can then be converted into the leaching efficiency of specific metals / elements using Eq. (4) by multiplying the mineral element composition (E^m) as measured by EPMA with the simulated cumulative mineral leaching result at each time $\left(\sum_t A_t^m\right)$ then added with the other mineral phase that bears the same element. Then it was divided with the total element as characterized by MLA ($\sum_m E^m\ x\ A_{total}^m$).

$$Leaching\ efficiency_{(Au,Ag,Te)}\ (\%) = \frac{\sum_m \sum_t E^m\ x\ A_t^m}{\sum_m E^m\ x\ A_{total}^m}\ x\ 100\% \quad (4)$$

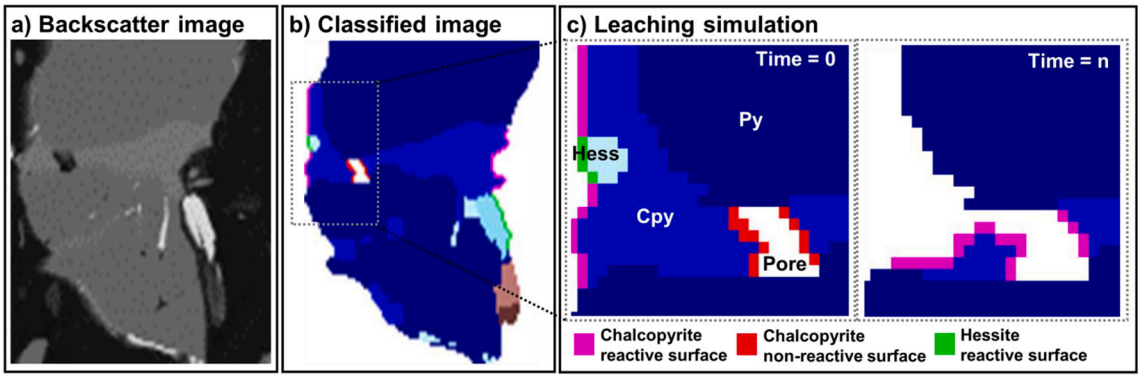

Fig. 2. Illustration of the leaching simulation. (a) Backscattered electron (BSE) image of a particle, (b) mineral classification using MLA that shows pyrite (Py, dark blue), chalcopyrite (Cpy, blue), hessite (Hess, light blue), Fe-oxide (light brown), chlorite (dark brown) and pore space (white). (c) Labelled reactive surface area (green and pink) and non-reactive surface area (red) at leaching time = 0 and after leaching time = n. (For interpretation of the references to colour in this figure legend, the reader is referred to the web version of this article.)

Within leaching, reactive surface area depends on the relationship of volume and surface area which varies over time due to the microstructures that changes during leaching. In classic shrinking core model (SCM) introduced by Yagi and Kunii, 1955, the relationship of volume and surface area was correlated over time using simplified solid such as sphere as the model. Compared to SCM, the proposed simulation in this study could have captured real microstructure including pores (Fig. 2) of the particle as provided by MLA and the relationship between volume and surface area by CT, which were not taken into consideration by SCM. The proposed simulation also open to the possibilities of using diffusion equation to control the leaching rate, if the diffusion laws were known.

2.6. Batch leaching experiments

Metal recoveries from bulk ore samples as a function of time were obtained by batch leaching experiments using ethaline solution with iodine. Leaching was carried out using the same experimental conditions as used for single particle leaching (500 rpm and 50 °C) and a liquid to solid (l/s) mass ratio of 10: 1. Two experiments were done, one using 7.15 g and another using 7.16 g of the sulfide concentrate by adapting the procedure described by Zürner and Frisch (2019). One milliliter of solution was sampled directly from the leaching container using polyamide syringes coupled with a 0.2 μm filter at leaching times of 0.25, 0.75, 2, 3, 4, 6, 24, 48 and 96 h of leaching time. The total solid weight lost in the filter was measured for each sampling step, which was accounted for during the calculation of metal recoveries. The maximum amount of particles lost due to filtering was 0.61 g and 0.66 g for each

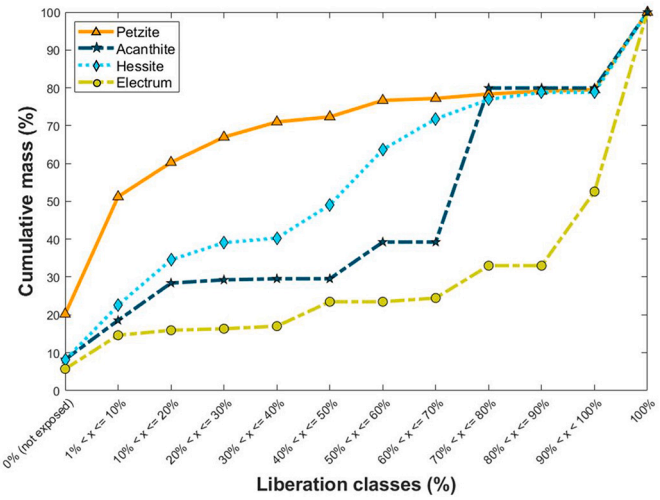

Fig. 4. Liberation by free surface area of the target Au-Ag-Te bearing minerals electrum, acanthite, hessite, and petzite.

experiment. Sampled leachates were analyzed by ICP-MS. Prior to analysis, the leachates were diluted 1:100000, 1:10000 and 1:1000 using 1% nitric acid for calibration. The calibration of the diluted solutions and sample solutions was done using Syngistix 2.4 software. Recovery was calculated based on ICP-MS analysis of the aliquots of the sulfide concentrate prior to leaching. The average recoveries of the two

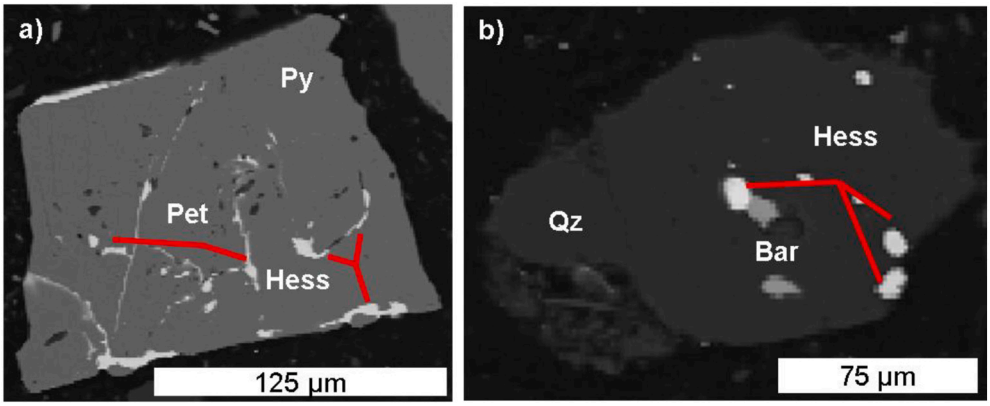

Fig. 3. BSE-SEM images illustrating typical occurrences of hessite and petzite in the sulfide concentrate (a) as short trails and infill in pyrite and (b) as minute grains of roundish shape enclosed in or attached to quartz. Py: pyrite; Pet: petzite; Hess: hessite; Qz: quartz; Bar: barite.

Table 2
Modal mineral composition of the sulfide concentrate giving the proportion of predominant minerals.

Minerals	Wt%	Area%
Pyrite	55.0	44.5
Quartz	19.5	28.9
Chalcopyrite	6.9	6.7
Galena	5.5	3.1
Orthoclase	4.4	6.1
Sphalerite	1.5	1.5
Chlorite	1.2	1.5
Calcite	1.1	1.6
Other	4.9	5.8
Total	100	100

Table 3
Calculated MAMA ratio of target Au-Ag-Te bearing minerals with 0% liberation by free surface area.

Major minerals	MAMA ratio*			
	Petzite	Acanthite	Hessite	Electrum
Quartz	0.13	0.53	0.29	0.48
Alkali Feldspar	0.16	2.29	1.72	–
Chlorite	0.10	–	–	0.67
Orthoclase	0.07	0.58	0.18	0.93
Pyrite	1.86	0.75	1.55	1.38
Chalcopyrite	0.37	0.37	0.22	–
Galena	1.22	1.54	1.19	0.16
Calcite	0.24	–	0.66	–
Silicates	0.04	–	0.23	3.63
Sulfides	0.18	–	0.93	2.63
Oxide	1.20	–	–	–
Sulfate	0.21	–	–	–

* Calculated preferential association of the Au-Ag-Te bearing minerals with 0% liberation as described by Kern et al., 2019. The calculated MAMA ratio shows that Au-Ag-Te bearing minerals were preferentially hosted by alkali feldspar, pyrite and galena, but electrum was preferentially associated with silicate and sulfides.

experiments was used to compare with the simulation results. Experimental leaching results for both experiments are collated in supplementary data.

3. Results

This section, report on the mineralogical composition of the sulfide concentrate feed sample (Figs. 3 and 4) as determined by MLA and EPMA. Then, the leaching results for single mineral particles studies (Fig. 5) and the arising mineral-specific dissolution rates are presented (Table 6). These experimentally determined dissolution rates are then used as input to the leaching simulation. Three particles were chosen as an example of the leaching simulation (Fig. 6) and results from the mineral leaching simulation of the sulfide concentrate is presented in Fig. 7. Finally, the expected leaching efficiency are compared with empirical batch leaching experiments (Fig. 8).

3.1. Mineralogical composition

The characterization of the sulfide concentrate by MLA shows it to be composed predominantly of pyrite, quartz, chalcopyrite, galena, orthoclase, sphalerite, chlorite, calcite (Table 2) and other sulfide, silicate, carbonate and oxide minerals present in less than 1 wt% abundance. The complete MLA data set can be found in the electronic supplement.

Hessite (Ag_2Te – 0.05 wt%), petzite (Ag_3AuTe_2–0.04 wt%), electrum (AuAg – 0.02 wt%), and acanthite (Ag_2S – 0.01 wt%) were identified as main ore minerals containing the three target metals (Au, Ag, Te). Petzite typically occurs as disseminated minute grains marked by poor liberation (Figs. 3 and 4). Half of all petzite grains were found to be poorly liberated between 0 and 10% liberation by free surface (Fig. 4) with ca. 20% not liberated at all. Hessite, acanthite and electrum on the other hand, have a higher degree of liberation compared to petzite, with almost two thirds of all grains between 10% and 100% liberated (Fig. 4). Grains with no liberation cannot directly be leached by the ethaline solution, unless the associated host mineral grain is dissolved first. However, the preferential association of the 0% liberation can be calculated using MAMA ratio (Kern et al., 2019) which is defined as the association of the mineral of interest divided by the abundance of the associated minerals in the sulfide concentrate. By doing so it becomes apparent that the target minerals: petzite, hessite, acanthite and electrum are preferentially hosted by alkali feldspar, pyrite and galena (Table 3). On the other hand, electrum is preferentially associated with several silicates (muscovite, chamosite, and orthoclase) and sulfides (sphalerite).

Table 4
Average elemental assays of electrum, petzite, hessite and acanthite.

Minerals	Elemental assay (% *w/w*)*				
	Au	Ag	Te	S	Total
Electrum	60.9	38.9	–	–	99.8
Petzite (Ag_3AuTe_2)	21.2	44.1	34.5	–	99.8
Hessite (Ag_2Te)	2.4	59.9	37.2	–	99.5
Acanthite (Ag_2S)	–	86.7	–	12.9	99.6

* As determined using EPMA, the values were averages from several analytical spots in different mineral grains.

Table 5
Concentration of gold, silver and tellurium in the digested sulfide concentrate.

Element	Concentration (g/t)*		
	Au	Ag	Te
ICP-MS	211	1268	460
Standard deviation	30	77	17

* Determined by ICP-MS, the value were averages of seven replicates measurement.

The chemical composition of precious metal from the four ore minerals is rather consistent, with the notable exception of electrum. Ten spot analyses of electrum by EPMA reveal distinct variations of the gold-silver content. On average, the electrum grains consist of 60.9 wt% gold and 38.9 wt% silver (Table 4) with a standard deviation for gold and for silver of 18.9 wt% and 17.9 wt%, respectively. Hessite was found to contain minor gold contents with 2.4 wt% on average (Table 4). In the bulk chemical analysis, average target element concentrations measured from the sulfide concentrate are summarized in Table 5. The complete EPMA and ICP-MS results are reported in the electronic supplement.

3.2. Dissolution rates from single particle leaching

All studied mineral grains, except pyrite, showed a distinct decrease in volume in the CT images in response to DES leaching (Fig. 5; Table 6). The pyrite grain did not show any detectable volume change for 90 h of exposure to ethaline solution. Leaching of chalcopyrite did result in a volume loss, but no marked decrease in surface area after 20 h of leaching. This can be attributed to an increase of roughness (Fig. 5f). Acanthite, hessite, sylvanite and galena all show volume loss associated with smoothing of the micro-scale roughness on the particle surface (Fig. 5b, c, d and e). The original galena grain, for example, has a distinct stair-case morphology that disappears. Dissolution rates calculated using Eq. (2), show higher selectivity of DES leaching towards the Au-Ag-Te bearing phase of acanthite, sylvanite, gold and hessite, as compared to the gangue minerals (galena, chalcopyrite, pyrite) with acanthite as the fastest and chalcopyrite with the slowest dissolution

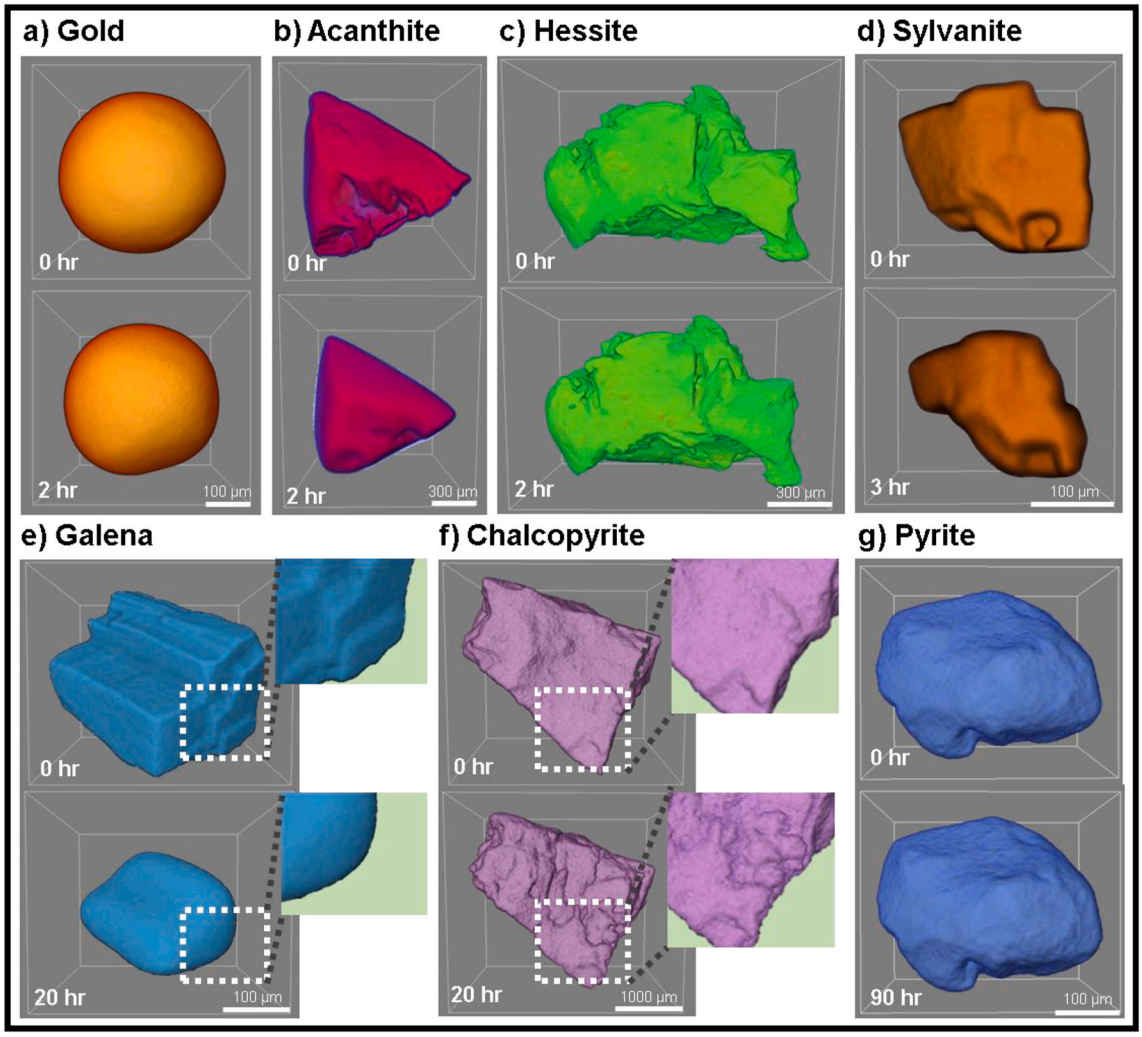

Fig. 5. 3D reconstructed CT images of the single particle leaching experiments. Surfaces of acanthite, hessite, sylvanite and galena grains are smoothed compared to an obvious increase in surface roughness observed for chalcopyrite in response to leaching. Note the apparent lack of dissolution of pyrite.

Table 6
The specific dissolution rates (k_norm) calculated from single particle leaching experiment.

Mineral (stoichiometric formula)	time (h)	Surface Area (μm^2)	Volume (μm^3)	k_norm ($\mu m\ h^{-1}$)
Acanthite (Ag_2S)	0	2.48×10^6	2.61×10^8	27.1
	2	1.55×10^6	1.52×10^8	
Hessite (Ag_2Te)	0	2.82×10^6	1.21×10^8	5.58
	2	2.83×10^6	8.93×10^7	
Sylvanite ($(Ag,Au)_2Te_4$)	0	1.68×10^5	4.54×10^6	5.46
	3	1.06×10^5	2.29×10^6	
Gold (Au)*	0	7.24×10^5	5.77×10^7	7.71
	2	6.35×10^5	4.72×10^7	
Galena (PbS)	0	4.34×10^5	1.92×10^7	1.81
	20	2.05×10^5	7.59×10^6	
Chalcopyrite ($CuFeS_2$)	0	1.29×10^6	8.59×10^7	0.821
	20	1.41×10^6	6.37×10^7	
Pyrite (FeS_2)	0	3.66×10^5	1.75×10^7	3.03×10^{-3}
	90	3.67×10^5	1.74×10^7	

* Note that a sphere of pure gold – rather than electrum – was used in the leaching experiment. It is assumed here that the dissolution rate of electrum and native gold will not be very different. See also results of Jenkin et al. (2016) for comparison.

rate.

3.3. Particle-based simulation of metal recoveries

The leaching behavior of 322,842 particles from the sulfide concentrate containing the target minerals was simulated using the dissolution rates reported in Table 6. The leaching behavior of three particles of different textural and mineralogical complexity is illustrated here as an examples (Fig. 6). The first of these particles (P1) is composed of non-liberated electrum (yellow) wedged between a quartz (red) and a hessite (light blue) grain, with the latter marked by high surface liberation (> 50%; Fig. 6a). Leaching thus first affects only the hessite grain. Progressive dissolution of hessite exposes the electrum grain after about 2 h. After another 2 h both electrum and hessite are fully dissolved. Particle P2 is marked by the occurrence of hessite and petzite (orange) grains that are enclosed in chalcopyrite (dark blue) (Fig. 6b). Due to the slow dissolution of chalcopyrite, approximately 6 h are necessary before hessite and petzite are liberated at surface and thus exposed to ethaline leaching. Leaching of these two grains is complete after another 6 h. Finally, particle P3 (Fig. 6c) is composed solely of electrum. Since the grain is fully liberated, it dissolves rather swiftly within less than 2 h.

Fig. 6 collates the results from the particle-based leaching simulation conducted for 322,842 individual particles. The results documented the leaching selectivity for target minerals compared to gangue minerals. This is illustrated by the time required to reach a final plateau in the

Table 7
Simulation results of expected mineral leaching at different leaching time.

Mineral	Simulated mineral leaching efficiency (%) at specific leaching times			
	2 h	4 h	24 h	96 h
Acanthite	92.1	92.1	92.1	92.9
Electrum	93.5	94.8	94.9	94.9
Hessite	83.7	92.2	93.6	93.6
Petzite	74.2	75.5	77.2	77.6
Galena	53.7	70.4	95.7	97.0
Chalcopyrite	27.7	45.5	89.5	98.2

leaching curve (Fig. 7). Acanthite and electrum reach more than 90% recovery after less than 2 h of leaching, hessite and petzite reach a recovery of 92% and 75% respectively after 4 h (Table 7). The fact that petzite recovery remains low compared to the other target minerals is simply an expression of unusually poor liberation (Fig. 4) and the association of petzite with non leachable gangue minerals (Table 3). For similar reasons it comes as no surprise that none of the target minerals reaches 100% mineral leaching. For example, 8.2% and 5.7% of all acanthite and electrum grains, respectively, have 0% surface liberation at the onset of the leaching experiment (Fig. 4) and are completely enclosed in either pyrite and quartz, two gangue minerals that remain unaffected by ethaline leaching. Because ethaline is unable to leach such inclusions, the acanthite and electrum mineral leaching will remain well below 100%. The simulation suggests that ethaline leaching is all but completed after only few hours for the ore minerals containing Ag, Au and Te, whereas the dissolution of galena and chalcopyrite will reach a plateau only after 24 h of leaching duration. By the end of the simulation, all studied minerals reach leaching recoveries of at least 90%, with the notable exception of petzite and, of course, the pyrite that remains entirely unaffected by the leaching process.

Element recoveries of gold, silver, and tellurium from both simulation and empirical batch leaching experiments are similar (Fig. 8). However, during the initial stages of the leaching process there is a significant difference between simulation results and empirical test work for the silver recovery, with the batch leaching experiments exhibiting slower leaching kinetics and up to 16% less recovery as compared to the simulation results (Table 8). This discrepancy in the recovery of silver decreases through time so that at 96 h is less than 5%. As for gold and tellurium, the leaching efficiencies from simulation and batch tests increase very quickly reaching more than 80% after only after 2 h, followed by a slow increase over 96 h of leaching time. The differences between experiment and simulation are less than 4% at 96 h.

4. Discussion

The leaching efficiency curves of the simulation and batch leaching experiments are generally in good agreement. Especially the leaching curves for gold and tellurium closely followed the prediction of the simulated leaching process. Minor deviations (Table 8) might have different reasons, including 1) distinct differences in mineral composition for the target minerals between those grains used in single particle leaching experiments and those actually present in the studied sulfide concentrate; 2) differences in leaching rates between monomineralic grains (used to determine the dissolution rate) and the minerals actually present in complex associations in the sulfide concentrate; 3) stereological bias of 2D images used for the simulation; and 4) complex ion exchange or secondary precipitation during the leaching process. Yet, given the compositional complexity of the sulfide concentrate and the leaching process, the agreement between empirical batch leaching experiments and the particle-based simulation for multiple values elements may be regarded as excellent.

Despite the agreement between empirical tests and simulation, there are still some important aspects that can be improved for future simulation efforts. The first aspect concepts the geometry of the particles and the roughness of the surface of grains are known to affect the dissolution rate of a mineral (Godinho and Stack, 2015; Noiriel et al., 2018). The effect of these parameters in the leaching can also be investigated with this method. For instance, the corners and edges of the particles have higher dissolution rates compared to flat particle surfaces as seen on the close up galena particle (Fig. 5e). Therefore, measured rates are an average for the entire surface, thus the rates are expected to change through time due to the progressive form evolution of the solid during leaching. Additionally, due to the different origin of the mineral samples leached in the single particle and batch leaching experiment may lead to different dissolution rates of the minerals. That is because the minerals used in single particle leaching might have slight variations of crystal structure (e.g. crystal defects) and composition relative to the minerals present in the ore. This is especially striking for the man-made gold sphere vs natural electrum grains. In fact, EPMA results also shows electrum can have a wide variability of gold-silver contents (solid solution in the precious metal alloy with varying relative abundances, see Table 4).Since the dissolution rates are relatively fast, those factors are assumed to not affect the overall rate significantly, although future experiments should be done to test these assumptions.

A second aspect concerns the possible stereological bias from MLA 2D images that may lead to an underestimation of grain size and overestimation of surface liberation, especially for minerals with low abundance. Such bias also can lead to deviations of mineral leaching between simulation and batch leaching (Fig. 7). Miss-interpretation of 2D non-reactive surfaces that could be exposed to the fluid in 3D, would cause longer time needed to reach the maximum recovery plateau. Statistical correction e.g. using the bootstrap method (Blannin et al., 2021) may be used to at least assess this error in order to improve the statistical robustness of the leaching simulation results.

The total leaching of target minerals did not reach 100% in both simulations (Fig. 7) and batch leaching experiments (Fig. 8). This is in good agreement with expectations since not all of the ore mineral grains are liberated (Fig. 4). Two examples are shown in Fig. 3, where the target tellurides: hessite and petzite are trapped inside insoluble minerals of pyrite or quartz. These mineral grains will not be dissolved during leaching. Liberation classes for the ore minerals (Fig. 4) confirm that some grains of ore minerals have no surface exposure prior to leaching. Only those enclosed in leachable host minerals (galena, chalcopyrite) will ultimately be recovered. The relative preference of such

Table 8
Comparison of element leaching efficiency from simulation and batch leaching experiments (**Δ**) at specific times.*

Leaching efficiency (%) at specific time intervals		2 h		4 h		24 h		96 h	
		%	Δ	%	Δ	%	Δ	%	Δ
Gold	Simulation	90.7	4.7	92.1	2.9	92.9	5.2	93.1	1.4
	Experiment	86		89.2		87.7		91.7	
Silver	Simulation	61.8	15.5	66.0	13.9	66.8	12.1	67.0	4.4
	Experiment	46.3		52.1		54.7		62.6	
Tellurium	Simulation	86.5	5.3	91.3	0.9	93.0	2.9	93.3	3.1
	Experiment	91.8		90.4		95.9		96.4	

* Experiment values corresponds to the average between 2 independent batch leaching experiments stirred at 500 rpm for 96 h at 50 °C with l/s ratio of 10.

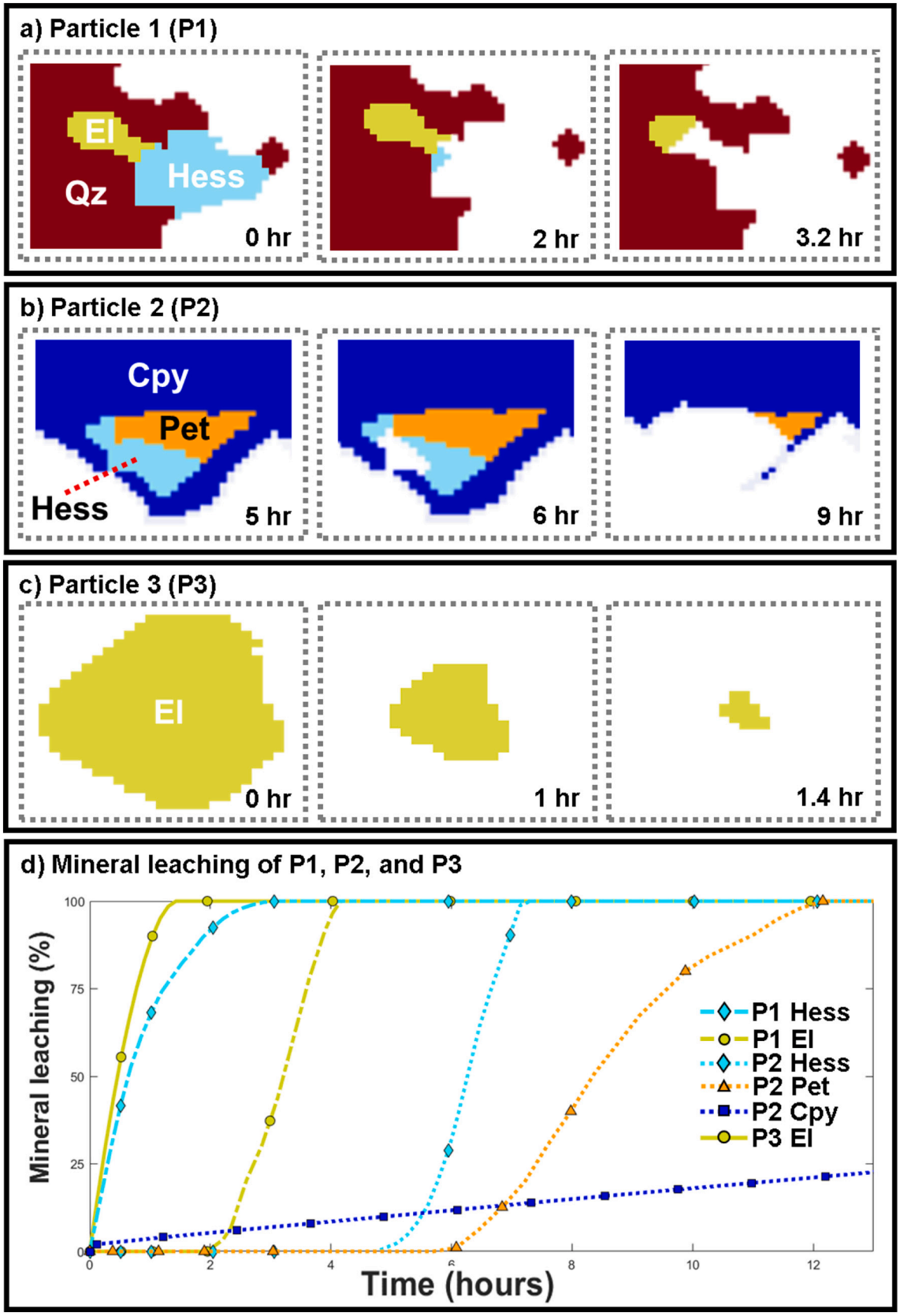

Fig. 6. Simulated leaching behavior of three selected ore particles. (a) Particle 1 (P1) contains electrum (El, yellow) as inclusion inside quartz (Qz, red) and hessite (Hess, light blue), (b) particle 2 (P2) comprises of hessite and petzite (Pet, orange) enclosed in chalcopyrite (Cpy, dark blue) matrix, (c) particle 3 (P3) is a monomineralic (i.e. fully liberated) electrum particle and (d) the cumulative mineral leaching plot of electrum, hessite, petzite, and chalcopyrite as simulated for particles P1, P2 and P3. (For interpretation of the references to colour in this figure legend, the reader is referred to the web version of this article.)

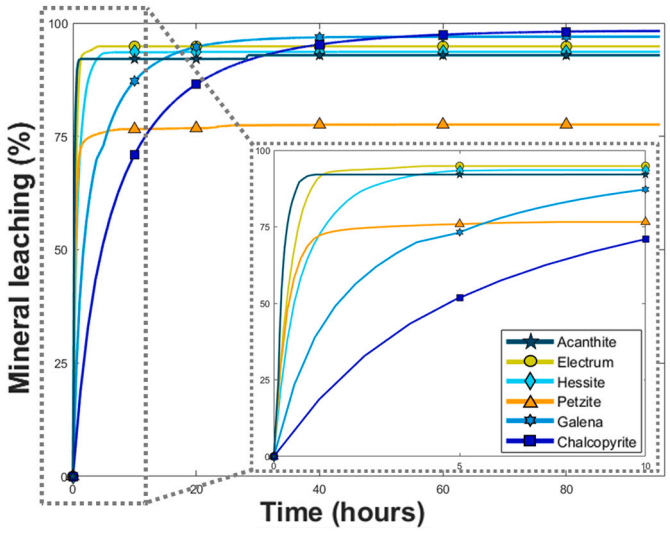

Fig. 7. Cumulative mineral leaching over 96 h of leaching simulation of acanthite, electrum, hessite, petzite, galena, and chalcopyrite for 322,842 particles.

associations is aptly expressed by the MAMA ratio (Table 3), which is an index that quantifies genetic and geometallurgical relationships and illustrates the strongly preferred association between minerals. The relative abundance of such inclusions in slowly dissolving host minerals readily explains the time required for petzite and hessite to reach their recovery plateau as compared to the well liberated electrum and acanthite (Figs. 7 and 4). Liberation hence changes during the leaching (Fig. 6a and b). This highlights the importance of considering initial particle compositions and changes of particle compositions during the leaching process – rather than only considering bulk compositions prior and after leaching.

The most obvious and only really relevant difference between simulations and empirical batch leaching test is that recorded for the recovery of Ag in the first few hours of batch leaching (Fig. 8). This initial difference is greatly diminished during the latter stages of the leaching experiment and can be attributed to the behavior of Ag during leaching. In ethaline solutions, Ag is known to forms $AgCl_2^-$ and $AgCl_3^{2-}$ complexes (Hartley et al., 2014). Similar complexes with iodine are known from other solvents. We regard it as very likely that such complexes also form under the conditions of the experiments conducted in this study. Silver concentrations in the batch leaching experiments did not exceed the solubility of the silver halides overall (0.2 mol L^{-1} for AgCl (Abbott et al., 2011)). Still, we deem it likely that poorly soluble AgCl and AgI precipitates may have formed due to local supersaturation on the surface of Ag-rich mineral grains. The evidently delayed recovery of Ag would then record the formation of Ag-halide precipitates, followed by slow dissolution of these precipitate. Additionally, the leached silver may affect the leaching rate of other minerals (Senanayake, 2008). Therefore, further understanding of the speciation of elements in the ethaline leaching medium could further improve the reproducibility of the model.

5. Conclusion

The workflow proposed in this paper is suited to observe and to quantify the effects of selectively leaching specific minerals / solid phase from multiphase particles. The workflow can be used to study as well as to predict the effectiveness and selectivity of leaching of certain minerals / solid phase from a complex mixture. Results can be directly translated into element recoveries achieved by leaching. The case study of the selective leaching of Au, Ag, and Te by DES from a sulfide concentrate from the Cononish Mine (Scotland) aptly illustrated the robustness of the

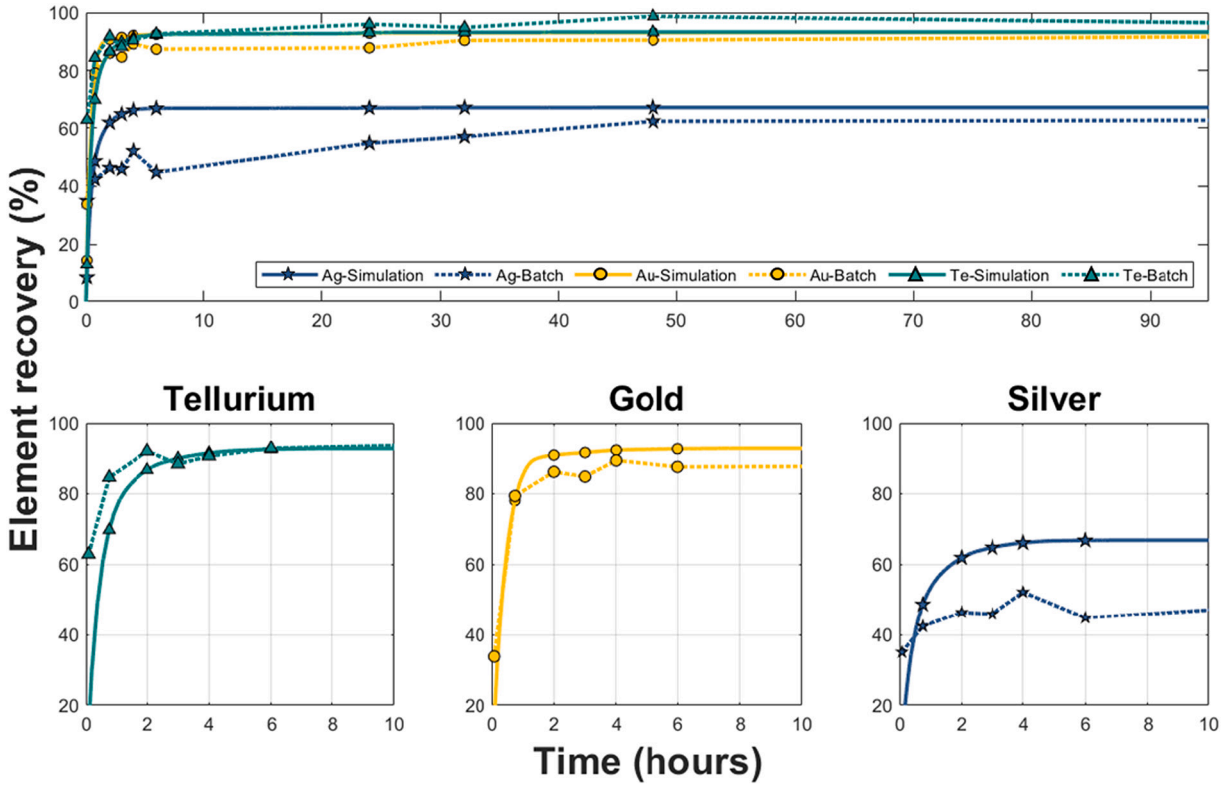

Fig. 8. Comparison between leaching efficiency of tellurium, gold and silver from the leaching simulation (continuous line) and the average batch leaching experiment (dotted line) stirred at 500 rpm for 96 h at 50 °C with l/s ratio of 10. (For interpretation of the references to colour in this figure legend, the reader is referred to the web version of this article.)

workflow. Ore minerals carrying the targeted metals were first identified by SEM-based image analysis and then characterized by electron microprobe analysis. Dissolution rates of the target minerals in the selected DES were determined by observing volumetric changes of monomineralic particles by CT. These rates were then applied to 2D images of particles obtained by SEM-based image analysis to simulate mineral leaching and element recovery based on the observed composition and textural relations. The simulation result are within 5% error compared to empirical batch leaching results, suggesting that the proposed workflow yields accurate results. The approach may well be transferred to other industrial leaching technologies where mineralogically complex feed materials are leached, including well established aqueous leaching technologies, such as those based on acids or cyanide.

Funding

This work was part of the ION4RAW project that received funding from the European Union's Horizon 2020 research and innovation program under grant agreement 815748.

CRediT authorship contribution statement

Chandra Widyananda Winardhi: Conceptualization, Methodology, Software, Validation, Investigation, Formal analysis, Writing – original draft, Visualization. **Jose Ricardo da Assuncao Godinho:** Conceptualization, Methodology, Writing – review & editing, Supervision. **Cindytami Rachmawati:** Investigation. **Isabelle Duhamel Achin:** Formal analysis, Writing – review & editing. **Ainhoa Unzurrunzaga Iturbe:** Formal analysis. **Gero Frisch:** Writing – review & editing, Supervision. **Jens Gutzmer:** Writing – review & editing, Supervision.

Declaration of Competing Interest

The authors declare that they have no known competing financial interests or personal relationships that could have appeared to influence the research reported in this paper.

Acknowledgements

The authors gratefully acknowledge Wardell Armstrong and Chris Sangster (Scotgold Resources) for providing the sulfide concentrate samples, Laurent Bailly and Guillaume Wille (BRGM) for electron microprobe measurements, the Geoscientific Collections of the TU Bergakademie Freiberg for providing the single gold-silver-telluride minerals samples, Roland Würkert (HIF-HZDR) for sample preparation, Kai Bachmann (HIF-HZDR) and Sabine Gilbricht (TUBAF) for MLA measurements as well as Laura Sanchez Cupido (Tecnalia) and Sabrina Beutner (IRE-HZDR) for ICP-MS analyses.

Appendix A. Supplementary data

Supplementary data to this article can be found online at https://doi.org/10.1016/j.hydromet.2022.105869.

References

Abbott, A.P., Capper, G., Davies, D.L., Rasheed, R.K., Tambyrajah, V., 2003. Novel solvent properties of choline chloride/urea mixtures. Chem. Commun. 1, 70–71. https://doi.org/10.1039/B210714G.

Abbott, A.P., Boothby, D., Capper, G., Davies, D.L., Rasheed, R.K., 2004. Deep eutectic solvents formed between choline chloride and carboxylic acids: versatile alternatives to ionic liquids. J. Am. Chem. Soc. 126 (29), 9142–9147. https://doi.org/10.1021/ja048266j.

Abbott, A.P., Capper, G., Davies, D.L., McKenzie, K.J., Obi, S.U., 2006. Solubility of metal oxides in deep eutectic solvents based on choline chloride. J. Chem. Eng. Data 51 (4), 1280–1282. https://doi.org/10.1021/je060038c.

Abbott, A.P., Frisch, G., Garrett, H., Hartley, J., 2011. Ionic liquids form ideal solutions. Chem. Commun. 47 (43), 11876–11878. https://doi.org/10.1039/C1CC14801J.

Abbott, A.P., Harris, R.C., Holyoak, F., Frisch, G., Hartley, J., Jenkin, G.R., 2015. Electrocatalytic recovery of elements from complex mixtures using deep eutectic solvents. Green Chem. 17 (4), 2172–2179. https://doi.org/10.1039/C4GC02246G.

Ancey, M., Bastenaire, F., Tixier, R., 1978. Proc. Summer School St. Martin-d'Herres. ed F Maurice (Orsay, France: Les Editions de Physique), pp. 319–343.

Anthony, M.T., Flett, D.S., 1994. Hydrometallurgy—an environmentally sustainable technology?. In: Hydrometallurgy, 94. Springer, Dordrecht, pp. 13–26. https://doi.org/10.1007/978-94-011-1214-7_2.

Blannin, R., Frenzel, M., Tuşa, L., Birtel, S., Ivăşcanu, P., Baker, T., Gutzmer, J., 2021. Uncertainties in quantitative mineralogical studies using scanning electron microscope-based image analysis. Miner. Eng. 167, 106836 https://doi.org/10.1016/j.mineng.2021.106836.

Cononish Project : Scotgold Resources Ltd, 2021. https://www.scotgoldresources.com/projects/cononish-project/ (accessed 4 June 2021).

Dávila-Pulido, G.I., Salinas-Rodríguez, A., Carrillo-Pedroza, F.R., González-Ibarra, A.A., Méndez-Nonell, J., Garza-García, M., 2021. Leaching kinetics of electronic waste for the recovery of copper: rate-controlling step and rate process in a multisize particle system. Int. J. Chem. Kinet. 53 (3), 379–389. https://doi.org/10.1002/kin.21450.

Dewanckele, J., De Kock, T., Boone, M.A., Cnudde, V., Brabant, L., Boone, M.N., Jacobs, P., 2012. 4D imaging and quantification of pore structure modifications inside natural building stones by means of high resolution X-ray CT. Sci. Total Environ. 416, 436–448. https://doi.org/10.1016/j.scitotenv.2011.11.018.

Fandrich, R., Gu, Y., Burrows, D., Moeller, K., 2007. Modern SEM-based mineral liberation analysis. Int. J. Miner. Process. 84 (1–4), 310–320. https://doi.org/10.1016/j.minpro.2006.07.018.

Gaydardjiev, S.S., 1998. Hydrometallurgy of precious metals: Effects on the environment. In: Mineral Processing and the Environment. Springer, Dordrecht, pp. 257–280. https://doi.org/10.1007/978-94-017-2284-1_13.

Godinho, J.R., Stack, A.G., 2015. Growth kinetics and morphology of barite crystals derived from face-specific growth rates. Cryst. Growth Des. 15 (5), 2064–2071. https://doi.org/10.1021/cg501507p.

Godinho, J.R.A., Piazolo, S., Evans, L., 2014. Simulation of surface dynamics during dissolution as a function of the surface orientation: Implications for non-constant dissolution rates. Earth and Planet. Sci. Lett. 408, 163–170. https://doi.org/10.1016/j.epsl.2014.10.018.

Godinho, J.R.A, Piazolo, S., Evins, L.Z., 2012. Effect of surface orientation on dissolution rates and topography of CaF2. Geochim. Cosmochim. Acta 86, 392–403. https://doi.org/10.1016/j.gca.2012.02.032.

Godinho, J.R.A, Gerke, K.M., Stack, A.G., Lee, P.D., 2016. The dynamic nature of crystal growth in pores. Sci. Rep. 6 (1), 1–7. https://doi.org/10.1038/srep33086.

Godinho, J.R.A., Kern, M., Renno, A.D., Gutzmer, J., 2019. Volume quantification in interphase voxels of ore minerals using 3D imaging. Miner. Eng. 144, 106016 https://doi.org/10.1016/j.mineng.2019.106016.

Godinho, J.R.A, Westaway-Heaven, G., Boone, M.A., Renno, A.D., 2021. Spectral tomography for 3D element detection and mineral analysis. Minerals 11 (6), 598. https://doi.org/10.3390/min11060598.

Godinho, J.R.A, Withers, P.J, 2018. Time-Lapse 3D imaging of calcite precipitation in a microporous column. Geochimica et cosmochimica acta 222, 156–170. https://doi.org/10.1016/j.gca.2017.10.024.

Hartley, J.M., Ip, C.M., Forrest, G.C., Singh, K., Gurman, S.J., Ryder, K.S., Frisch, G., 2014. EXAFS study into the speciation of metal salts dissolved in ionic liquids and deep eutectic solvents. Inorg. Chem. 53 (12), 6280–6288. https://doi.org/10.1021/ic500824r.

Heinig, T., Bachmann, K., Tolosana-Delgado, R., Van Den Boogaart, G., Gutzmer, J., 2015, September. Monitoring gravitational and particle shape settling effects on MLA sampling preparation. In: Proceedings of IAMG, pp. 200–206.

Ilhan, S., Akgün, D., 2021. Leaching kinetics of Mo, Ni, and Al oxides from spent nickel–molybdenum hydrodesulfurization catalyst in H2SO4 solution. J. Sustain. Metal. 7 (2), 470–480. https://doi.org/10.1007/s40831-021-00351-5.

Jenkin, G.R., Al-Bassam, A.Z., Harris, R.C., Abbott, A.P., Smith, D.J., Holwell, D.A., Stanley, C.J., 2016. The application of deep eutectic solvent ionic liquids for environmentally-friendly dissolution and recovery of precious metals. Miner. Eng. 87, 18–24. https://doi.org/10.1016/j.mineng.2015.09.026.

Kalair, A., Abas, N., Saleem, M.S., Kalair, A.R., Khan, N., 2021. Role of energy storage systems in energy transition from fossil fuels to renewables. Energy Stor. 3 (1), e135 https://doi.org/10.1002/est2.135.

Kern, M., Kästner, J., Tolosana-Delgado, R., Jeske, T., Gutzmer, J., 2019. The inherent link between ore formation and geometallurgy as documented by complex tin mineralization at the Hämmerlein deposit (Erzgebirge, Germany). Mineral. Deposita 54 (5), 683–698. https://doi.org/10.1007/s00126-018-0832-2.

Lin, Q., Dobson, D.J., Lee, P.D., Neethling, S.J., 2016. Modelling particle scale leach kinetics based on X-ray computed micro-tomography images. Hydrometallurgy 162, 25–36. https://doi.org/10.1016/j.hydromet.2016.02.008.

Lin, Q., Neethling, S.J., Courtois, L., Dobson, K.J., Lee, P.D., 2016. Multi-scale quantification of leaching performance using X-ray tomography. Hydrometallurgy 164, 265–277. https://doi.org/10.1016/j.hydromet.2016.06.020.

Merlet, C., 1992. Quantitative electron probe microanalysis: new accurate Φ (ρz) description. In: Electron Microbeam Analysis. Springer, Vienna, pp. 107–115. https://doi.org/10.1007/978-3-7091-6679-6_8.

Merlet, C., 1994. An accurate computer correction program for quantitative electron probe microanalysis. Microchim. Acta 114 (1), 363–376. https://doi.org/10.1007/BF01244563.

Miehe, G., Kupčík, V., 1971. Die Kristallstruktur des Bi (Bi 2 S 3) 9 J 3. Naturwissenschaften 58 (4), 219. https://doi.org/10.1007/BF00591851.

Noiriel, C., Luquot, L., Madé, B., Raimbault, L., Gouze, P., van der Lee, J., 2009. Changes in reactive surface area during limestone dissolution: an experimental and modelling study. Chem. Geol. 265 (1–2), 160–170. https://doi.org/10.1016/j.chemgeo.2009.01.032.

Noiriel, C., Oursin, M., Saldi, G., Haberthür, D., 2018. Direct determination of dissolution rates at crystal surfaces using 3D X-ray microtomography. ACS Earth Space Chem. 3 (1), 100–108. https://doi.org/10.1021/acsearthspacechem.8b00143.

Noiriel, C., Oursin, M., Daval, D., 2020. Examination of crystal dissolution in 3D: a way to reconcile dissolution rates in the laboratory? Geochim. Cosmochim. Acta 273, 1–25. https://doi.org/10.1016/j.gca.2020.01.003.

Picot, P., Pierrot, R., 1963. La roquesite, premier minéral d'indium: CuInS2. Bull. Mineral. 86 (1), 7–14. https://doi.org/10.3406/bulmi.1963.5607.

Radošević, K., Bubalo, M.C., Srček, V.G., Grgas, D., Dragičević, T.L., Redovniković, I.R., 2015. Evaluation of toxicity and biodegradability of choline chloride based deep eutectic solvents. Ecotoxicol. Environ. Saf. 112, 46–53. https://doi.org/10.1016/j.ecoenv.2014.09.034.

Rodriguez, N.R., Machiels, L., Onghena, B., Spooren, J., Binnemans, K., 2020. Selective recovery of zinc from goethite residue in the zinc industry using deep-eutectic solvents. RSC Adv. 10 (12), 7328–7335. https://doi.org/10.1039/D0RA00277A.

Saldi, G.D., Voltolini, M., Knauss, K.G., 2017. Effects of surface orientation, fluid chemistry and mechanical polishing on the variability of dolomite dissolution rates. Geochim. Cosmochim. Acta 206, 94–111. https://doi.org/10.1016/j.gca.2017.02.007.

Schulz, B., Merker, G., Gutzmer, J., 2019. Automated SEM mineral liberation analysis (MLA) with generically labelled EDX spectra in the mineral processing of rare earth element ores. Minerals 9 (9), 527. https://doi.org/10.3390/min9090527.

Senanayake, G., 2008. A review of effects of silver, lead, sulfide and carbonaceous matter on gold cyanidation and mechanistic interpretation. Hydrometallurgy 90 (1), 46–73. https://doi.org/10.1016/j.hydromet.2007.09.013.

Smith, E.L., Abbott, A.P., Ryder, K.S., 2014. Deep eutectic solvents (DESs) and their applications. Chem. Rev. 114 (21), 11060–11082. https://doi.org/10.1021/cr300162p.

Wang, L., Putnis, C.V., 2020. Dissolution and precipitation dynamics at environmental mineral interfaces imaged by in situ atomic force microscopy. Accounts of Chemical Research 53 (6), 1196–1205. https://doi.org/10.1021/acs.accounts.0c00128.

Wills, B.A., Finch, J.A., 2015. Wills' mineral processing technology: an introduction to the practical aspects of ore treatment and mineral recovery. Butterworth-Heinemann. https://doi.org/10.1016/B978-0-08-097053-0.00005-4.

Yagi, S., Kunii, D., 1955, January. Studies on combustion of carbon particles in flames and fluidized beds. In: Symposium (international) on Combustion, Vol. 5. Elsevier, pp. 231–244. https://doi.org/10.1016/S0082-0784(55)80033-1. No. 1.

Zhou, J., Sui, H., Jia, Z., Yang, Z., He, L., Li, X., 2018. Recovery and purification of ionic liquids from solutions: a review. RSC Adv. 8 (57), 32832–32864. https://doi.org/10.1039/C8RA06384B.

Zürner, P., Frisch, G., 2019. Leaching and selective extraction of indium and tin from zinc flue dust using an oxalic acid-based deep eutectic solvent. ACS Sustain. Chem. Eng. 7 (5), 5300–5308. https://doi.org/10.1021/acssuschemeng.8b06331.